Interconversion between Free Charges and Bound Excitons in 2D Hybrid Lead Halide Perovskites

Gélvez-Rueda, María C.; Hutter, Eline M.; Cao, Duyen H.; Renaud, Nicolas; Stoumpos, Constantinos C.; Hupp, Joseph T.; Savenije, Tom J.; Kanatzidis, Mercouri G.; Grozema, Ferdinand C.

DOI
10.1021/acs.jpcc.7b10705

Publication date
2017

Document Version
Final published version

Published in
The Journal of Physical Chemistry C

THE JOURNAL OF PHYSICAL CHEMISTRY C

Article

Cite This: J. Phys. Chem. C 2017, 121, 26566-26574

pubs.acs.org/JPCC

Interconversion between Free Charges and Bound Excitons in 2D Hybrid Lead Halide Perovskites

María C. Gélvez-Rueda,[†] Eline M. Hutter,[†] Duyen H. Cao,[‡] Nicolas Renaud,[†] Constantinos C. Stoumpos,[‡] Joseph T. Hupp,[‡] Tom J. Savenije,[†] Mercouri G. Kanatzidis,[‡] and Ferdinand C. Grozema*[,†]

[†]Section Optoelectronic Materials, Department of Chemical Engineering, Delft University of Technology, Van der Maasweg 9, 2629 HZ Delft, The Netherlands

[‡]Department of Chemistry and Argonne−Northwestern Solar Energy Research (ANSER) Center, Northwestern University, 2145 Sheridan Road, Evanston, Illinois 60208, United States

Supporting Information

ABSTRACT: The optoelectronic properties of hybrid perovskites can be easily tailored by varying their components. Specifically, mixing the common short organic cation (methylammonium (MA)) with a larger one (e.g., butyl ammonium (BA)) results in 2-dimensional perovskites with varying thicknesses of inorganic layers separated by the large organic cation. In both of these applications, a detailed understanding of the dissociation and recombination of electron−hole pairs is of prime importance. In this work, we give a clear experimental demonstration of the interconversion between bound excitons and free charges as a function of temperature by combining microwave conductivity techniques with photoluminescence measurements. We demonstrate that the exciton binding energy varies strongly (between 80 and 370 meV) with the thickness of the inorganic layers. Additionally, we show that the mobility of charges increases with the layer thickness, in agreement with calculated effective masses from electronic structure calculations.

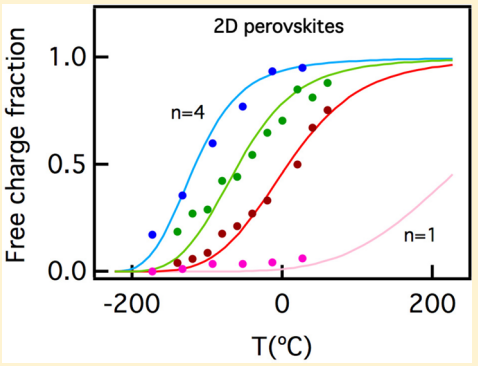

INTRODUCTION

Organic−inorganic halide perovskites are intensively studied materials for optoelectronic applications such as photovoltaic solar cells, light-emitting diodes, and lasers.[1,2] Their attractiveness is a result of their ease of preparation and tunable optoelectronic properties.[3] Solar cells based on three-dimensional (3D) perovskites, AMX_3 (with A = Cs, $CH_3NH_3^+$, $HC(NH_2)_2^+$, M = Pb^{2+}, Sn^{2+}, Ge^{2+}; X = I^-, Br^-, Cl^-), have surpassed an overall power conversion efficiency of 22%.[4,5] Recently, the family of layered 2D Ruddlesden−Popper perovskite materials has gained significant attention because of their improved moisture stability, promising device efficiency, and intriguing optical properties.[6−13] 2D perovskites are layered materials that are formed by partially or fully replacing the small methylammonium (MA) cation with a larger cation, reducing the 3D perovskite framework to 2D layered structures due to steric hindrance.[3] A detailed understanding of these materials, especially the photogeneration and transport of charges, is currently lacking.[2] 2D hybrid perovskites with a large organic cation were extensively studied in the 90s for their unique quantum-well structure that enhances exciton confinement beyond predictions for 2D systems.[14,15] This additional confinement has been attributed to the large difference between the dielectric constants of the large organic "barrier" and the inorganic "well".[9,14,16−18] Generation of bound and long-lived (Wannier−Mott) excitons with exciton binding energies of several hundreds of meV, renders these materials good candidates for photoluminescent applications such as lasers and light-emitting diodes (LDs and LEDs)[19,20] and nonlinear optical[21] and polaritonic devices.[22−26] However, in many cases, they exhibit inefficient luminescence at room temperature possibly due to thermal quenching of the excitons or strong exciton−phonon interactions.[12,27−32]

An interesting feature of 2D hybrid perovskites is the high tunability of their chemical and physical properties. This can be achieved by exchanging the halogen[6] or by introducing both large and small organic cations and controlling the thickness of $[(MA)_{n-1}Pb_nI_{3n+1}]^{2-}$ slabs through the value of n.[7,8,33−36] Thin films of 2D perovskites are solution-processable and exhibit a higher stability than 3D perovskites under ambient conditions.[21,7,36] Highly efficient solar cells (PCE of 12.5%)[11] and LEDs[12] (EQE of 8.8%) have been reported recently. These devices were based on 2D perovskites with butylammonium (BA) and phenylethylammonium (PEA) as the bulky organic cations, respectively. A key property of optoelectronic materials that characterize their performance in both solar cells and LEDs

Received: October 30, 2017
Revised: November 3, 2017
Published: November 3, 2017

DOI: 10.1021/acs.jpcc.7b10705
J. Phys. Chem. C 2017, 121, 26566−26574

is the exciton binding energy that determines the probability of dissociation of excitons and the recombination of charges. For 3D hybrid perovskites, there has been a considerable debate on the nature of photoexcited excitons as well as the exciton binding energy values.[17,37−44]

In this work, we have studied the dynamics of charges and excited states in a series of 2D Ruddlesden−Popper lead iodide perovskites: $(BA)_2(MA)_{n-1}Pb_nI_{3n+1}$ (n = 1−5). The 2D structure consists of single (n = 1) or multiple layers of $[PbI_6]^{4-}$ octahedral containing the small MA cation $[(MA)_{n-1}Pb_nI_{3n+1}]^{2-}$ separated by the longer BA cations (Figure 1).[7]

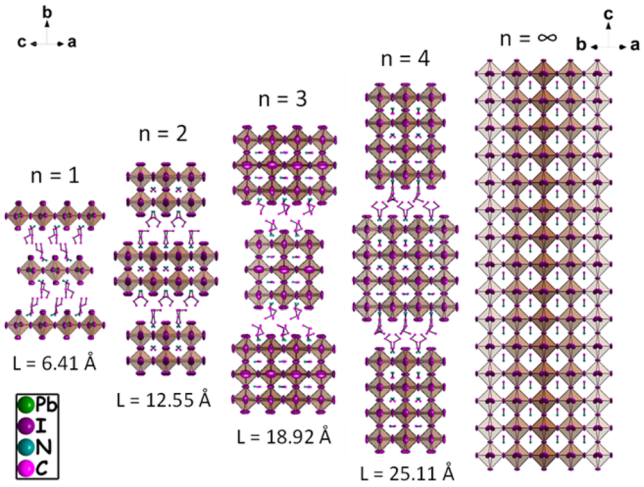

Figure 1. Crystal structures of 2D and 3D hybrid lead iodide perovskites, $(BA)_2(MA)_{n-1}Pb_nI_{3n+1}$, extending from n = 1 to n = ∞. The thickness of the layers is defined by n.

By combining distinct time-resolved microwave conductivity (TRMC) techniques, we performed a detailed temperature study of the mobility (irradiation with high-energy electrons) and exciton dissociation (laser excitation) in these materials. These measurements reveal that at low temperature the mobility of charges increases but the generation of "free charges" that are not coulombically bound (i.e., nonexcitonic) is less efficient since the formation of Coulombically bound (Wannier−Mott) excitons is favored. This is accompanied by an increase in the fluorescence quantum yield that follows the opposite trend as observed for the fraction of free charges, i.e., higher quantum yields at low temperature. In this work, we show, for the first time, direct experimental evidence of the interconversion of excitons into free charges on going from low to high temperatures. This interconversion process is governed by an exciton binding energy that strongly depends on the thickness of the number of inorganic layers (n), ranging from ∼370 meV for n = 1 to ∼80 meV for n = 4. The combination of these TRMC techniques also demonstrates the strong dependence of the mobility, exciton dissociation, and lifetime of charges on the thickness of the slabs (n). The mobility of charges clearly increases with the slab thickness. This is consistent with previously shown band broadening with n thickness[45] and our own DFT calculations that predict a decrease in the effective mass of holes. In addition, the exciton dissociation becomes more efficient and the lifetime longer with increased layer thickness, which is a direct result of the reduced Coulombic interactions between electrons and holes (exciton binding energy). This work gives a unique insight in the dissociation properties of excitons in perovskites materials by using a complementary combination of microwave conductivity techniques.

EXPERIMENTAL SECTION

Starting Materials. All chemicals were purchased from Sigma-Aldrich and used as received. Methylammonium iodide (MAI) was synthesized by neutralizing equimolar amounts of a 57% w/w aqueous hydriodic acid (HI) and 40% w/w aqueous methylamine (CH_3NH_2) (pH ∼ 7). The white precipitate was collected by evaporation of the solvent using rotary evaporation at 60 °C under reduced pressure.

2D Hybrid Perovskites Synthesis. $(BA)_2(MA)_3Pb_4I_{13}$ (n = 4). PbO powder (2232 mg, 10 mmol) was dissolved in a mixture of 57% w/w aqueous HI solution (10.0 mL, 76 mmol) and 50% aqueous H_3PO_2 (1.7 mL, 15.5 mmol) by heating to boiling under constant magnetic stirring for about 5 min, forming a bright yellow solution. Subsequent addition of solid CH_3NH_3I (1192 mg, 7.5 mmol) to the hot yellow solution initially caused the precipitation of a black powder which rapidly redissolved under stirring to afford a clear bright yellow solution. In a separate beaker, n-$CH_3(CH_2)_3NH_2$ (248 μL, 2.5 mmol) was neutralized with HI 57% w/w (5 mL, 38 mmol) in an ice bath, resulting in a clear pale yellow solution. Addition of the n-$CH_3(CH_2)_3NH_3I$ solution to the $MAPbI_3$ solution initially produced a black precipitate which subsequently dissolved under heating the combined solution to boiling. The stirring was then discontinued, and the solution was allowed to cool to room temperature during which time black rectangular-shaped plates started to crystallize. The precipitation was deemed to be complete after ∼2 h. The crystals were isolated by suction filtration and thoroughly dried under reduced pressure.

For a detailed description of the synthesis of the remaining compounds in the series, refer to Stoumpos et al.[10]

Preparation of PR-TRMC Sample Holders. A small amount of material (∼45 mg) is placed in a polyether ether ketone (PEEK) holder and filled by pouring droplets of poly methyl methacrylate (PMMA) dissolved in chlorobenzene at a concentration of 10 mg/mL every 10 min until the perovskite material is fully covered by PMMA. Then the sample holder is allowed to sit overnight to ensure the complete evaporation of the solvent. The PMMA filling is done in order to protect the samples from moisture and air and diminish the background conductivity of the material (which affects the PR-TRMC measurements). The cavity of the PEEK holder is 6 × 3 × 2 mm^3. The PEEK block with the perovskite sample is placed inside a rectangular waveguide copper cell of 14 mm length and 7.1 × 3.55 mm^2 of front side. The copper top wall was reduced to 0.4 mm thickness to minimize the attenuation of the electron beam. The walls of the cell were gold-plated via a redox exchange of copper with gold in order to make the cell chemically inert.

PR-TRMC Measurements. PR-TRMC measurements involve the generation of charge carriers through irradiation by a short pulse of high-energy electrons (3 MeV) and the monitoring of the changes in conductivity due to mobile charge carriers using high frequency microwaves (28−38 GHz).[46−48] The high-energy electron pulse ionizes the charges in the material via Coulomb interactions. These interactions are caused by the rapidly changing electric field of the electrons in the pulse. This mechanism is similar to the oscillating electric field of a photon. However, it has a larger penetration depth

DOI: 10.1021/acs.jpcc.7b10705
J. Phys. Chem. C 2017, 121, 26566−26574

and higher energy (~20 eV) that results in the generation of a uniform concentration of charge carriers far away from each other. The thermal relaxations of the charges that are produced in this way occurs well within a nanosecond, and hence, it does not influence recombination of the charges.

If the free charge carriers generated in this way are mobile, this results in a fractional absorption of microwave power reflected by the cell that is directly proportional to the change in conductivity of the material studied (eq 3).[46−48]

$$\frac{\Delta P}{P} = A\Delta\sigma \tag{3}$$

The fractional change in the microwave power, $\Delta P/P$, and the sensitivity factor, A, are frequency dependent as the overlap of the electric field strength of the microwaves in the samples changes with frequency. In addition, interference effects of the incoming and reflected waves in the cell can also vary with frequency. The experimental frequency dependence of $\Delta P/P$ can be fitted with an analytical expression to determine the dielectric constant, ε, and change in conductivity, $\Delta\sigma$.[46−48] Information about trapping, recombination processes, and carrier lifetimes in the material can be determined from the temporal decay kinetics of the transients varying the initial concentration of charges in the material (by varying the length of the pulse).

The change in conductivity initially increases during the pulse as mobile charge carriers are generated and gradually decreases after the pulse as the charges recombine or get trapped in time. The overall time response of the PR-TRMC set up is limited by the rise time of the detector diode and the length of the excitation pulse but is less than 1 ns, i.e., much shorter than the lifetime of the conductivity signals. The mobility of the charges is determined from the change in the conductivity ($\Delta\sigma$) if the charge carrier concentration at the end of the electron pulse (N_p) according to eq 4.[46−48] Since it is not possible to selectively generate positive or negative charges, the mobility determined by PR-TRMC technique is the sum of the electron and hole mobilities

$$\Delta\sigma = e\sum N_p(0)\mu = e(n_n\mu_n + n_p\mu_p) \tag{4}$$

where $N_p(0)$ is the initial concentration of charge carriers at the end of the pulse, μ is the sum of the mobilities for electrons and holes (eq 5), and $N_p(0)$ is a function of the mass of material (m), volume of the sample holder (V_{sh}), irradiation energy deposited in the sample (D), and of the radiation−ionization energy required for the generation of an electron−hole pair (E_p).

$$N_p(0) = \frac{D}{E_p \times 1.6 \times 10^{-19}\frac{J}{eV}}\frac{m}{V_{sh}} \tag{5}$$

Here, D is proportional to the electron density of the material and for perovskites has been determined to be ~1 J/kg/nC. The latter is derived from previous radiation dosimetry experiments.[46−48] E_p has been determined according to Klein's theoretical model and Alig's equation for semiconductor materials (eq 6), which relates it to the band gap of the material, phonon losses, and the residual kinetic energy.[49,50]

$$E_p = 2.73E_g + 0.55\ (\text{eV}) \tag{6}$$

In the PR-TRMC set up, the cell is contained in a cryostat in which the temperature can be varied between −150 and +200 °C. The temperature was maintained for ~15 min before doing actual measurement was performed in order to ensure the equilibrium of the system. The irradiation intensity was varied between pulse lengths of 200 ps and 2 ns for each temperature at a frequency of 32 GHz. The frequency scan (28−38 GHz) fits were measured at a pulse length of 500 ps. We emphasize that the radiation doses used in our experiment are not sufficient to cause significant radiation damage. Klein-Kedem et al.[51] found that perovskites solar cells are unstable under absorbed radiation power ~10^9 W cm^{-3}. The radiation power that is absorbed in our experiments is 3 orders of magnitude lower (~10^6 W cm^{-3}). In addition, in our radiation experiment we test approximately micrometer size crystals instead of thin films. Bulk samples and single crystals are more stable under irradiation conditions than films.

Preparation of Thin Films. Quartz substrates were cleaned with oxygen plasma-treated immediately prior to film fabrication. Fabrication of the 2D hybrid perovskites thin films was carried out in a nitrogen-filled glovebox. The precursor solutions were prepared by mixing 100 mg of bulk material in 1.5 mL of anhydrous dimethylformamide (DMF). The solutions were filtered using a 0.45 μm pore size filter before spin coating. For the spin-coating step, 100 μL of the perovskite solution was spin coated on the substrate for 30 s at 8000 rpm. Directly after spin coating, the films were annealed at 100 °C for 2 min.

Photoconductivity Measurements. Thin films on quartz substrates were placed in a sealed resonance cavity inside a nitrogen-filled glovebox. The time-resolved microwave conductivity (TRMC) technique was used to measure the change in microwave (8−9 GHz) power after pulsed excitation (repetition rate 10 Hz) of the OMHPs at 520, 620, 760, 780, and 775 nm for n = 1, 2, 3, 4, and ∞, respectively. The photoexcitation-induced change in microwave power is related to the change in conductance ΔG by a sensitivity factor K:

$$\frac{\Delta P(t)}{P} = -k\Delta G(t) \tag{7}$$

The rise of ΔG is limited by the width of the laser pulse (3.5 ns fwhm) and the response time of our microwave system (18 ns). The slow repetition rate of the laser of 10 Hz ensures full relaxation of all photoinduced charges to the ground state before the next laser pulse hits the sample. The product of the yield of free charges (x) and the mobility ($\sum\mu = \mu_e + \mu_h$) was calculated from the maximum change in photoconductance ΔG_{max}:

$$x\Sigma\mu = \frac{\Delta G_{max}}{I_0\beta e F_A} \tag{8}$$

In eq 3, I_0 is the number of photons per unit area per pulse, β is the ratio of the inner dimensions of the microwave cell, e is the elementary charge, and F_A is the fraction of light absorbed by the sample at the excitation wavelength. Before and during the photoconductance measurements, the samples were not exposed to moisture or air to prevent degradation.[52,53]

Optical Characterization. Absorption spectra were recorded with a PerkinElmer Lambda 1050 spectrophotometer equipped with an integrated sphere. The thin films were placed under an angle of 10° inside the sphere to detect the total fraction of reflected and transmitted photons (FR+T). From here, we calculated the fraction of absorbed light (FA):

$$F_A = 1 - F_{T+R} \tag{9}$$

DOI: 10.1021/acs.jpcc.7b10705
J. Phys. Chem. C 2017, 121, 26566−26574

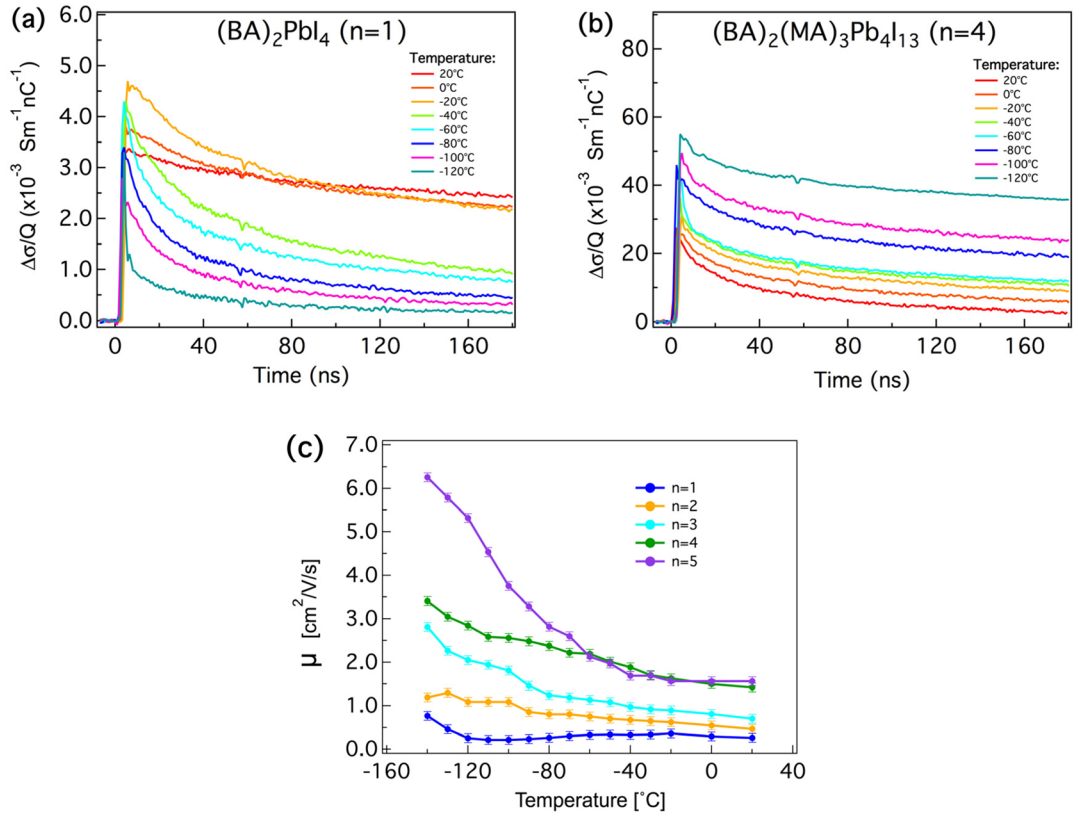

Figure 2. Conductivity transients for (a) $(BA)_2PbI_4$ (n = 1) and (b) $(BA)_2(MA)_3Pb_4I_{13}$ (n = 4) bulk materials at different temperatures. (c) Mobility of 2D perovskites: $(BA)_2PbI_4$ (n = 1), $(BA)_2(MA)Pb_2I_7$ (n = 2), $(BA)_2(MA)_2Pb_3I_{10}$ (n = 3), $(BA)_2(MA)_3Pb_4I_{13}$ (n = 4) and $(BA)_2(MA)_4Pb_5I_{16}$ (n = 5) at different temperatures.

Photoluminescent Measurements. Thin films on quartz substrates were placed in a sealed cryostat under nitrogen flow. The PL emission spectra were recorded using an Edinburgh LifeSpec spectrometer equipped with a single photon counter. The 2D films were excited at 405 nm with a picosecond pulsed diode laser (Hamamatsu, M8903−01, $I_0 \sim 1 \times 10^{12}$ photons/cm^2, repetition rate 0.1 MHz).

DFT Calculations. All DFT calculations were performed with the BAND program included in the Amsterdam Density Functional suite. During the calculation, the experimental geometry was used. The electronic structure calculations were performed using a triple-ζ basis set (TZP) and without using frozen cores. The PBEsol functional was used to account for exchange and correlation. Relativistic effects were included via a scalar correction of the ZORA. The effective masses were calculated using the internal capabilities of BAND.

RESULTS AND DISCUSSION

Temperature Dependence of Charge Mobility. The crystal structures of the 2D perovskites studied here are shown in Figure 1. The materials were synthesized using our previously reported recipe, reacting stoichiometric amounts of $C_4H_9NH_2$, CH_3NH_3I, and PbI_2 in excess HI/H_3PO_2 acid solution, filtering by suction filtration, and drying in a vacuum oven.[7] The purity of all materials was confirmed by X-ray diffraction, UV−vis spectroscopy, and photoluminescence measurements.[7,10]

The mobility was studied by pulse-radiolysis time-resolved microwave conductivity (PR-TRMC). In these measurements, charge carriers are generated through irradiation by a short pulse of very high energy electrons (3 MeV). The change in conductivity due to the generation of mobile charge carriers is monitored by measuring the absorption of high frequency microwaves (28−38 GHz).[46−48] A unique aspect of the use of high-energy electrons is the generation of a uniform concentration of free charge carriers with an average energy transfer of ∼20 eV per ionization event. This high energy leads to free electrons and holes that are generated with a spatial separation larger than the thickness of the $[(MA)_{n-1}Pb_nI_{3n+1}]^{2-}$ slab, regardless of the exciton binding energy.[46−48] We emphasize that this method of generating charges is very different from the laser photoconductivity excitation used in TRMC and terahertz spectroscopy. With laser excitation, charge carriers are generated very close to each other with a nonuniform concentration profile.[52] In the highly confined 2D materials, excitation by a laser will generate bound excitons where the electron and hole reside in the same $[(MA)_{n-1}Pb_nI_{3n+1}]^{2-}$ slab. As a consequence, the latter measurements are sensitive to the magnitude of exciton binding energies.

Radiation-induced conductivity transients obtained by PR-TRMC measurements for $(BA)_2PbI_4$ (n = 1) and $(BA)_2(MA)_3Pb_4I_{13}$ (n = 4) at different temperatures are shown in Figure 2. The conductivity normalized by the charge in the pulse ($\delta\sigma/Q$) rises during the irradiation pulse as mobile charge carriers are generated. Subsequently, the conductivity decreases after the pulse as the charges recombine or become trapped. In Figure 2a it is seen that for $(BA)_2PbI_4$ (n = 1), the lifetime is very long at room temperature but decreases at lower temperatures. The long lifetime at room temperature implies that the electron and the corresponding hole are indeed

DOI: 10.1021/acs.jpcc.7b10705
J. Phys. Chem. C 2017, 121, 26566−26574

generated in separate $[(MA)_{n-1}Pb_nI_{3n+1}]^{2-}$ slabs, resulting in a very slow bimolecular recombination across the organic layer between the slabs (see TRMC transients as a function of the initial concentration in Figure S1). The change in the decay kinetics occurs when the temperature decreases below 0 °C. Interestingly, this coincides with a structural phase transition (around 0 to −17 °C).[54] This structural change, leading to more disorder of BA, causes a blue shift in the bandgap[54] and higher exciton peak energy.[9] Figure 2b represents the radiation-induced conductivity of the $(BA)_2(MA)_3Pb_4I_{13}$ (n = 4) compound. The behavior of the remaining 2D materials is similar to the n = 4 compound and is included in Figure S2. Unlike the single-layered n = 1 material, the conductivity and charge carrier lifetime gradually increase as the temperature decreases. This has recently also been reported for the 3D $MAPbX_3$ perovskites.[55] This shows that the presence of the MA significantly affects the charge dynamics in these materials.

The mobility of the charges can be determined from the change in the conductivity ($\Delta\sigma$) if the charge carrier concentration at the end of the electron pulse is known (see methods). The mobility values for our 2D series $(BA)_2(MA)_{n-1}Pb_nI_{3n+1}$, n = 1−5, are plotted as a function of temperature in Figure 2c. We observe a clear increase in the mobility as the thickness increases from n = 1 to 4. Interestingly, for n = 5, the mobility is higher than that of n = 4 only at temperatures below −50 °C. We have performed DFT band structure calculations, summarized in Figure S3, that relate this increase in mobility to changes in the band structure. As the thickness increases, the effective mass of the holes steadily decreases, explaining the observed increase in mobility. This is in agreement with DFT calculations that demonstrated band broadening with the increase of the layer thickness.[45] Furthermore, the mobility increases as the temperature decreases. The temperature-dependent mobility follows an electron−phonon scattering transport mechanism in the n = 1−4 compounds (Figure S4). However, this trend deviates in n = 5 at temperature below −80 °C. We have shown recently that in $MAPbX_3$ (X = I, Br, Cl), the trend in mobility as a function of temperature deviates from electron−phonon scattering transport below the β/γ phase transition.[55] This deviation (abrupt increase in mobility and lifetime) was attributed to the restriction of the rotational freedom of the MA cations on going through a structural phase transition. In n = 5, the mobility and lifetime (Figures S4 and S5) considerably increase at temperatures below −100 °C. These results suggest that as the thickness increases the charge dynamics approach the behavior of their 3D analogue. Possibly, as the $[(MA)_{n-1}Pb_nI_{3n+1}]^{2-}$ slab becomes thicker there is more freedom for the MA cations to rotate. This dynamic disorder affects the structure (as observed in DSC measurements (Figures S6 and S7)) and the charge dynamics (as seen in PR-TRMC measurements) in a similar way as in 3D hybrid perovskites.

Photogeneration of Mobile Charges. From the above measurements, we have obtained information on the temperature dependence of the charge carrier mobility. In order to gain insight into the dissociation of photogenerated excitons into free charges, we proceeded with microwave photoconductivity measurements on thin films of the same materials. In these measurements, charge carriers are generated using laser photoexcitation instead of an electron pulse. As discussed above, in such an experiment electron−hole pairs are generated in a single slab. Due to the strong confinement for n = 1 (E_b = ~ 370 meV),[14,15,18] it is likely that a large fraction of the photogenerated species exist as bound excitons at room temperature and these do not contribute to the conductivity signal. Therefore, the result of such measurements is not a direct measure of the charge mobility but the product of charge mobility ($\sum\mu = \mu_e + \mu_h$) and quantum yield of charge formation (x). However, from the PR-TRMC measurements, we already know how the mobility varies with temperature and thickness of the slabs. Therefore, combining this information with photoconductivity TRMC we can obtain information on the yield of exciton dissociation, which is intrinsically related to the exciton binding energy.

The normalized photoconductivity and the conductivity half-lifetime are plotted as a function of the thickness (n) in Figure 3. It is clear that the photoconductivity and half-lifetime depend strongly on the thickness. As the slab thickness increases, the photoconductivity and half-lifetime also increase. The increase in photoconductivity is a result of increases in both the charge mobility mobility ($\sum\mu$) *and* the quantum yield of charge formation (x). However, the change in charge mobility with slab thickness is much smaller than the observed variation in photoconductivity. This indicates that the exciton dissociation also varies strongly with the slab thickness. As shown in Figure 3b, the lifetime is very short for n = 1 as electrons and holes are generated in the same slab and can recombine easily. The exciton binding energy decreases as the slab thickness increases,

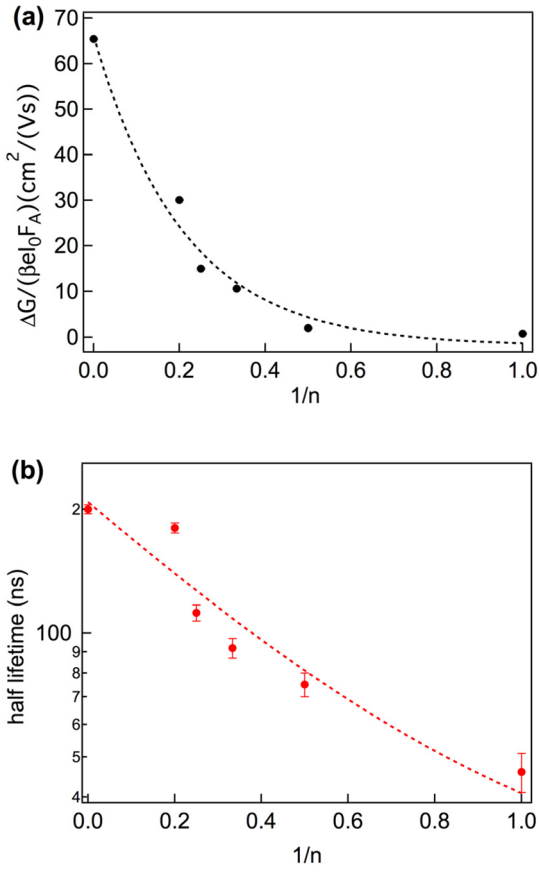

Figure 3. Photoconductivity (a) and half-lifetime (b) dependence of 2D perovskites on the thickness of the $[(MA)_{n-1}Pb_nI_{3n+1}]^{2-}$ slabs at room temperature. Excited at the emission wavelength. The dotted lines are a guide to the eye. In panel (a) the error bars are smaller than the symbols.

DOI: 10.1021/acs.jpcc.7b10705
J. Phys. Chem. C 2017, 121, 26566−26574

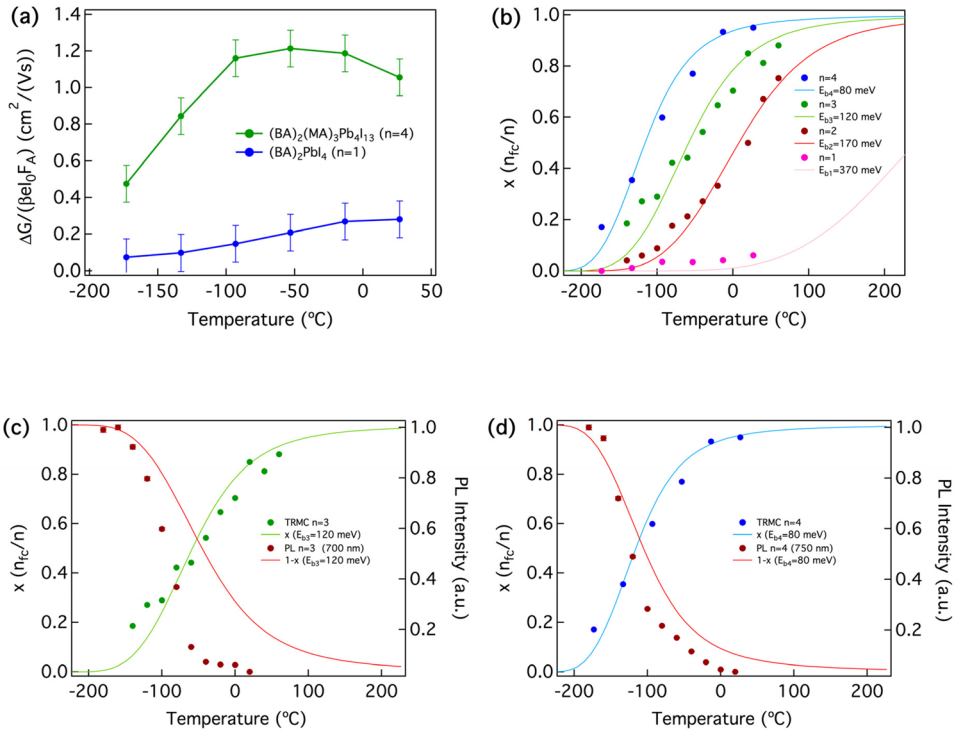

Figure 4. Photoconductivity of (a) $BAPbI_4$ (n = 1) and $(BA)_2(MA)_3Pb_4I_{13}$ (n = 4) at different temperatures; samples were excited at 473 nm with a photon intensity of 2×10^{11} cm^{-2}. (b) Fraction of free charges as a function of temperature. The full lines are modeled using the Saha equation with an excitation density of 5×10^{14} cm^{-3}. The symbols indicate the experimental estimates. (c, d) Fraction of free charges estimated from TRMC measurements (green and blue symbols) and the fraction of bound excitons obtained from PL (red symbols) for (c) $(BA)_2(MA)_2Pb_3I_{10}$ (n = 3) and (d) $(BA)_2(MA)_3Pb_4I_{13}$ (n = 4) at different temperatures. Excited at 405 nm with a photon intensity of ~1×10^{12} cm^{-3}. The full lines are modeled using the Saha equation with excitation densities of 8×10^{14} cm^{-3}(PL) and 5×10^{14} cm^{-3} (TRMC). The error bars in panels b–d are not visible because they are smaller than the symbols.

resulting in an increase in the yield of free charges and also in the lifetime. The lifetimes measured with the different TRMC techniques differ by 1 order of magnitude due to the influence of the exciton binding energy. In the photoconductivity TRMC, the free charges generated by laser excitation are closer to each other. As a consequence, they recombine faster due to the strong Coulombic interactions between electrons and holes. In addition, the lifetimes measured by TRMC are longer than fluorescence (0.03–0.5 ns)[56,57] and terahertz (<1 ps)[58] lifetimes reported in literature. The conductivity lifetimes do not correspond to fluorescence measurements as the species that are detected in both measurements are different. The fluorescence lifetime is determined by band-to-band recombination of electrons and holes (radiative recombination) that can either exist as free charges or as bound electron–hole pairs. In the case of TRMC measurements, we selectively detect mobile free carriers that either recombine with each other (radiatively) or via trap states. At room temperature, the pure 2D $(BA)_2PbI_4$ exhibits mostly bound excitons after excitation, not free charges, that recombine very fast due to the high exciton binding energy. This is why the PL lifetime is orders of magnitude shorter that in the TRMC experiments. In the case of the very short (<1 ps) free carrier lifetime determined by terahertz measurements, this lifetime is so short as in terahertz measurements the excitation density is very high (>10^{17} cm^{-3}).[58] In our TRMC experiments, the excitation density is orders of magnitude lower (~10^{14}–10^{16} cm^{-3}).

To examine how the formation of free charges depends on temperature, we have performed temperature-dependent photoconductivity measurements. The maximum photoconductivity is shown as a function of temperature for n = 1 and n = 4 in Figure 4a (see Figure S8 for n = 2 and 3). Interestingly, the photoconductivity decreases as the temperature decreases. However, as discussed above, the charge carrier mobility was shown to increase with decreasing temperature. Therefore, these measurements directly indicate that at low temperature fewer free charges are formed upon photoexcitation; i.e., the yield of exciton dissociation is lower.

A clearer picture of the relative yield of free charges as a function of temperature is obtained when the photoinduced conductivity, $[x\sum\mu]_{PC}$, is normalized by the mobility from the pulse radiolysis experiments, $\sum\mu_{PR}$ (eq 1).

$$x(T) = \frac{[x\sum\mu]_{PC}(T)}{\sum\mu_{PR}(T)} \quad (1)$$

It is important to note that this normalization gives the trend of x with temperature and not the absolute values. The large difference in the nature of the samples examined in the two techniques, polycrystalline powders in pulse radiolysis and thin spin-coated films in photoconductivity experiments, can result in different mobility values.[55] This makes it necessary to define the yield of dissociation at room temperature. We define each yield separately using theoretical values previously reported for a similar 2D perovskite (~4% for n = 1, ~50% for n = 2, ~85% for n = 3, and ~95% for n = 4).[44] These values are reasonable as for n = 1 the exciton binding energy is known to be very high (~370 meV[14,15,18,44]). This is consistent with the very low photoconductivity signals observed here. For n = 4, the yield is expected to be very close to 100% at room temperature,[11,12]

DOI: 10.1021/acs.jpcc.7b10705
J. Phys. Chem. C 2017, 121, 26566–26574

which is consistent with the almost constant photoconductivity at higher temperatures.

Theoretically, the yield of free charges can be estimated using the Saha equation. This equation relates the yield of free charges to the excitation density, effective mass of the exciton, temperature, and exciton binding energy (eq 2).

$$\frac{x^2}{1-x} = \frac{1}{n}\left(\frac{2\pi\mu k_B T}{h^2}\right)^{3/2} e^{-E_B/k_B T} \quad (2)$$

In Figure 4b, we compare the experimental yield of dissociation with a fit using the Saha equation with the effective mass obtained from DFT calculations and excitation densities around 5×10^{14} cm^{-3} to 1×10^{15} cm^{-3} (see the SI for a detailed description of this analysis). At high temperatures, the yield of dissociation is constant and steeply decreases as the temperature falls. Using this analysis, we estimate that the exciton binding energy is approximately 370 meV for n = 1, 170 meV for n = 2, 120 meV for n = 3, and 80 meV for n = 4. These values are smaller than those calculated by Koutselas et al. but are close to the experimental values determined from optical absorption spectra.[16,44,59]

The photoconductivity experiments clearly show a decrease in the yield of free charges. This should be accompanied by an increase in the yield of bound excitons and hence an increase in the fluorescence quantum yield at low temperatures. To confirm this, we have performed temperature-dependent photoluminescence measurements (Figure S9). The normalized photoluminescence intensities for the n = 3 and n = 4 materials are plotted as a function of temperature in parts c and d, respectively, of Figure 4. In addition, the experimental yield of dissociation obtained from our photoconductivity measurements and the fraction of free charges (x) and bound excitons ($1 - x$) obtained from the Saha equation are also included. In Figure 4c,d, we observed that for n = 3 and n = 4 both the photoluminescence intensity (related to the yield of bound excitons) and the dissociation yield closely follow the trend predicted by the Saha equation. In fact, the normalized photoluminescence intensity is almost exactly opposite to the decrease in the yield of free charges. In the case of n = 1 and n = 2, the normalized photoluminescence trend with temperature does not follow this trend so clearly (see Figure S10). Nevertheless, the relative fluorescence intensity increases as the temperature decreases, pointing to a larger fraction of bound excitons. This deviation from the simple behavior observed for n = 3 and n = 4 is likely to be the result of structural changes that can lead to changes in the nonradiative decay of the excitons.[12,27,28] This is consistent with photoluminescence quantum yield measurements in which for n = 1 the quantum yield is very low and have a maximum value for n = 3–5.[12] Moreover, the n = 1 and n = 2 compounds exhibit multiple bands in the emission spectrum that change in opposite ways with temperature (see Figure S9). The latter is currently not fully understood. Overall, the combination of the experiments presented here clearly shown the interconversion between excitons and free charges when the temperature is varied. This temperature behavior closely follows the trend predicted by the Saha equation. It should be noted that the we do not obtain information on the specific nature of the excitons; we merely observe the interconversion between mobile unbound charge carriers and Coulomb-bound excitons, which can either be freely moving in the material or bound to a defect. It was shown recently that edge states play an important role in the photogeneration of charges in exfoliated 2D perovskites.[60] Such edge states are expected to play a smaller role here due to the parallel orientation of the perovskite layers with respect to the substrate; it can not be excluded that the exciton binding energy that we obtain is influenced by this.

CONCLUSIONS

In this work, we have studied 2D $(BA)_2(MA)_{n-1}Pb_nI_{3n+1}$ Ruddlesden–Popper hybrid perovskites using two distinct microwave conductivity techniques with different pulsed excitation sources: high-energy electron pulse and laser photoexcitation. Our combined experimental results show a clear increase of the mobility of charge, the probability of exciton dissociation, and the lifetime of charges with the thickness of the $[(MA)_{n-1}Pb_nI_{3n+1}]^{2-}$ slabs. The increase in mobility is consistent with DFT calculations that show a decrease of the effective mass of holes. The larger exciton dissociation yield and longer lifetime of charges are explained by an increased dielectric shielding of the electron–hole interactions and hence a lower exciton binding energy. From temperature dependent microwave conductivity experiments the trend in the yield of exciton dissociation was obtained and analyzed in the framework of the Saha equation. This comparison shows that the exciton binding energies range between ~80 and ~370 meV depending on the thickness of the $[(MA)_{n-1}Pb_nI_{3n+1}]^{2-}$ slabs. Temperature-dependent photoluminescence experiments show that the free charges combine into bound excitons as the temperature is lowered. This results in an increased photoluminescence intensity with a temperature trend that is almost exactly opposite that in the yield of free charges.

ASSOCIATED CONTENT

Supporting Information

The Supporting Information is available free of charge on the ACS Publications website at DOI: 10.1021/acs.jpcc.7b10705.

Detailed PR-TRMC measurements (transients, mobility, half-lifetime), DSC measurements, DFT band structure calculations, photoconductivity and photoluminescent measurements, excitation densities analysis, and characterization measurements (XRD and absorption spectra) (PDF)

AUTHOR INFORMATION

Corresponding Author

*E-mail: f.c.grozema@tudelft.nl.

ORCID

Eline M. Hutter: 0000-0002-5537-6545
Constantinos C. Stoumpos: 0000-0001-8396-9578
Joseph T. Hupp: 0000-0003-3982-9812
Tom J. Savenije: 0000-0003-1435-9885
Mercouri G. Kanatzidis: 0000-0003-2037-4168
Ferdinand C. Grozema: 0000-0002-4375-799X

Notes

The authors declare no competing financial interest.

ACKNOWLEDGMENTS

The research leading to these results at Delft University of Technology has received funding from the European Research Council Horizon 2020 ERC Grant Agreement No. 648433 and The Netherlands Organization for Scientific Research (NWO)

DOI: 10.1021/acs.jpcc.7b10705
J. Phys. Chem. C 2017, 121, 26566–26574

under Echo Grant No. 712.014.007. The work at Northwestern University was supported as part of the Argonne−Northwestern Solar Energy Research (ANSER) Center, an Energy Frontier Research Center funded by the U.S. Department of Energy, Office of Science, Office of Basic Energy Sciences, under Award No. DE-SC0001059. D.H.C. acknowledges support from the Link Foundation through the Link Foundation Energy Fellowship Program.

REFERENCES

(1) Snaith, H. J. Perovskites: The Emergence of a New Era for Low-Cost, High-Efficiency Solar Cells. *J. Phys. Chem. Lett.* **2013**, *4*, 3623−3630.
(2) Brenner, T. M.; Egger, D. A.; Kronik, L.; Hodes, G.; Cahen, D. Hybrid Organic—Inorganic Perovskites: Low-Cost Semiconductors with Intriguing Charge-Transport Properties. *Nat. Rev. Mater.* **2016**, *1*, 15007.
(3) Mitzi, D. B. Synthesis, Structure, and Properties of Organic-Inorganic Perovskites and Related Materials. *Prog. Inorg. Chem.* **1999**, *48*, 1−121.
(4) Jeon, N. J.; Noh, J. H.; Yang, W. S.; Kim, Y. C.; Ryu, S.; Seo, J.; Seok, S. I. Compositional Engineering of Perovskite Materials for High-Performance Solar Cells. *Nature* **2015**, *517*, 476−480.
(5) NREL. *NREL Best Research-Cell Efficiencies*. https://www.nrel.gov/pv/assets/images/efficiency-chart.png (accessed 03/11/2017).
(6) Lanty, G.; Jemli, K.; Wei, Y.; Leymarie, J.; Even, J.; Lauret, J. S.; Deleporte, E. Room-Temperature Optical Tunability and Inhomogeneous Broadening in 2d-Layered Organic-Inorganic Perovskite Pseudobinary Alloys. *J. Phys. Chem. Lett.* **2014**, *5*, 3958−3963.
(7) Cao, D. H.; Stoumpos, C. C.; Farha, O. K.; Hupp, J. T.; Kanatzidis, M. G. 2d Homologous Perovskites as Light-Absorbing Materials for Solar Cell Applications. *J. Am. Chem. Soc.* **2015**, *137*, 7843−7850.
(8) Wu, X. X.; Trinh, M. T.; Zhu, X. Y. Excitonic Many-Body Interactions in Two-Dimensional Lead Iodide Perovskite Quantum Wells. *J. Phys. Chem. C* **2015**, *119*, 14714−14721.
(9) Yaffe, O.; Chernikov, A.; Norman, Z. M.; Zhong, Y.; Velauthapillai, A.; van der Zande, A.; Owen, J. S.; Heinz, T. F. Excitons in Ultrathin Organic-Inorganic Perovskite Crystals. *Phys. Rev. B: Condens. Matter Mater. Phys.* **2015**, *92*, 045414.
(10) Stoumpos, C. C.; Cao, D. H.; Clark, D. J.; Young, J.; Rondinelli, J. M.; Jang, J. I.; Hupp, J. T.; Kanatzidis, M. G. Ruddlesden−Popper Hybrid Lead Iodide Perovskite 2d Homologous Semiconductors. *Chem. Mater.* **2016**, *28*, 2852−2867.
(11) Tsai, H.; Nie, W.; Blancon, J. C.; Stoumpos, C. C.; Asadpour, R.; Harutyunyan, B.; Neukirch, A. J.; Verduzco, R.; Crochet, J. J.; Tretiak, S.; et al. High-Efficiency Two-Dimensional Ruddlesden-Popper Perovskite Solar Cells. *Nature* **2016**, *536*, 312−316.
(12) Yuan, M.; Quan, L. N.; Comin, R.; Walters, G.; Sabatini, R.; Voznyy, O.; Hoogland, S.; Zhao, Y.; Beauregard, E. M.; Kanjanaboos, P.; et al. Perovskite Energy Funnels for Efficient Light-Emitting Diodes. *Nat. Nanotechnol.* **2016**, *11*, 872−877.
(13) Milot, R. L.; Sutton, R. J.; Eperon, G. E.; Haghighirad, A. A.; Martinez Hardigree, J.; Miranda, L.; Snaith, H. J.; Johnston, M. B.; Herz, L. M. Charge-Carrier Dynamics in 2d Hybrid Metal−Halide Perovskites. *Nano Lett.* **2016**, *16*, 7001−7007.
(14) Tanaka, K.; Takahashi, T.; Kondo, T.; Umebayashi, T.; Asai, K.; Ema, K. Image Charge Effect on Two-Dimensional Excitons in an Inorganic-Organic Quantum-Well Crystal. *Phys. Rev. B: Condens. Matter Mater. Phys.* **2005**, *71*, 045312.
(15) Ishihara, T.; Takahashi, J.; Goto, T. Exciton-State in Two-Dimensional Perovskite Semiconductor (C10h21nh3)2pbi4. *Solid State Commun.* **1989**, *69*, 933−936.
(16) Ishihara, T. Optical-Properties of Pbi-Based Perovskite Structures. *J. Lumin.* **1994**, *60−61*, 269−274.
(17) Muljarov, E. A.; Tikhodeev, S. G.; Gippius, N. A.; Ishihara, T. Excitons in Self-Organized Semiconductor-Insulator Superlattices - Pbi-Based Perovskite Compounds. *Phys. Rev. B: Condens. Matter Mater. Phys.* **1995**, *51*, 14370−14378.
(18) Ishihara, T.; Takahashi, J.; Goto, T. Optical-Properties Due to Electronic-Transitions in 2-Dimensional Semiconductors (Cnh2n + 1nh3)2pbi4. *Phys. Rev. B: Condens. Matter Mater. Phys.* **1990**, *42*, 11099−11107.
(19) Hattori, T.; Taira, T.; Era, M.; Tsutsui, T.; Saito, S. Highly Efficient Electroluminescence from a Heterostructure Device Combined with Emissive Layered-Perovskite and an Electron-Transporting Organic Compound. *Chem. Phys. Lett.* **1996**, *254*, 103−108.
(20) Gebauer, T.; Schmid, G. Inorganic-Organic Hybrid Structured Led's. *Z. Anorg. Allg. Chem.* **1999**, *625*, 1124−1128.
(21) Kondo, T.; Iwamoto, S.; Hayase, S.; Tanaka, K.; Ishi, J.; Mizuno, M.; Ema, K.; Ito, R. Resonant Third-Order Optical Nonlinearity in the Layered Perovskite-Type Material (C6h13nh3)(2)Pbi4. *Solid State Commun.* **1998**, *105*, 503−506.
(22) Fujita, T.; Sato, Y.; Kuitani, T.; Ishihara, T. Tunable Polariton Absorption of Distributed Feedback Microcavities at Room Temperature (Vol, 57, Pg 12428, 1998). *Phys. Rev. B: Condens. Matter Mater. Phys.* **1998**, *58*, 7456−7456.
(23) Yablonskii, A. L.; Muljarov, E. A.; Gippius, N. A.; Tikhodeev, S. G.; Fujita, T.; Ishihara, T. Polariton Effect in Distributed Feedback Microcavities. *J. Phys. Soc. Jpn.* **2001**, *70*, 1137−1144.
(24) Brehier, A.; Parashkov, R.; Lauret, J. S.; Deleporte, E. Strong Exciton-Photon Coupling in a Microcavity Containing Layered Perovskite Semiconductors. *Appl. Phys. Lett.* **2006**, *89*, 171110.
(25) Wenus, J.; Parashkov, R.; Ceccarelli, S.; Brehier, A.; Lauret, J. S.; Skolnick, M. S.; Deleporte, E.; Lidzey, D. G. Hybrid Organic-Inorganic Exciton-Polaritons in a Strongly Coupled Microcavity. *Phys. Rev. B: Condens. Matter Mater. Phys.* **2006**, *74*, 235212.
(26) Lanty, G.; Lauret, J. S.; Deleporte, E.; Bouchoule, S.; Lafosse, X. Uv Polaritonic Emission from a Perovskite-Based Microcavity. *Appl. Phys. Lett.* **2008**, *93*, 081101.
(27) Chondroudis, K.; Mitzi, D. B. Electroluminescence from an Organic-Inorganic Perovskite Incorporating a Quaterthiophene Dye within Lead Halide Perovskite Layers. *Chem. Mater.* **1999**, *11*, 3028−3030.
(28) Dou, L. T.; Wong, A. B.; Yu, Y.; Lai, M. L.; Kornienko, N.; Eaton, S. W.; Fu, A.; Bischak, C. G.; Ma, J.; Ding, T. N.; et al. Atomically Thin Two-Dimensional Organic-Inorganic Hybrid Perovskites. *Science* **2015**, *349*, 1518−1521.
(29) Zhang, S.; Yi, C.; Wang, N.; Sun, Y.; Zou, W.; Wei, Y.; Cao, Y.; Miao, Y.; Li, R.; Yin, Y.; et al. Efficient Red Perovskite Light-Emitting Diodes Based on Solution-Processed Multiple Quantum Wells. *Adv. Mater.* **2017**, *29*, 1606600.
(30) Li, R. Z.; Yi, C.; Ge, R.; Zou, W.; Cheng, L.; Wang, N. N.; Wang, J. P.; Huang, W. Room-Temperature Electroluminescence from Two-Dimensional Lead Halide Perovskites. *Appl. Phys. Lett.* **2016**, *109*, 151101.
(31) Gauthron, K.; Lauret, J. S.; Doyennette, L.; Lanty, G.; Al Choueiry, A.; Zhang, S. J.; Brehier, A.; Largeau, L.; Mauguin, O.; Bloch, J.; et al. Optical Spectroscopy of Two-Dimensional Layered (C6h5c2h4-Nh3)2-Pbi4 Perovskite. *Opt. Express* **2010**, *18*, 5912−5919.
(32) Hong, X.; Ishihara, T.; Nurmikko, A. V. Dielectric Confinement Effect on Excitons in Pbi4-Based Layered Semiconductors. *Phys. Rev. B: Condens. Matter Mater. Phys.* **1992**, *45*, 6961−6964.
(33) Mitzi, D. B.; Wang, S.; Feild, C. A.; Chess, C. A.; Guloy, A. M. Conducting Layered Organic-Inorganic Halides Containing (110)-Oriented Perovskite Sheets. *Science* **1995**, *267*, 1473−1476.
(34) Smith, I. C.; Hoke, E. T.; Solis-Ibarra, D.; McGehee, M. D.; Karunadasa, H. I. A Layered Hybrid Perovskite Solar-Cell Absorber with Enhanced Moisture Stability. *Angew. Chem., Int. Ed.* **2014**, *53*, 11232−11235.
(35) Wu, X. X.; Trinh, M. T.; Niesner, D.; Zhu, H. M.; Norman, Z.; Owen, J. S.; Yaffe, O.; Kudisch, B. J.; Zhu, X. Y. Trap States in Lead Iodide Perovskites. *J. Am. Chem. Soc.* **2015**, *137*, 2089−2096.

DOI: 10.1021/acs.jpcc.7b10705
J. Phys. Chem. C 2017, 121, 26566−26574

(36) Tanaka, K.; Kondo, T. Bandgap and Exciton Binding Energies in Lead-Iodide-Based Natural Quantum-Well Crystals. *Sci. Technol. Adv. Mater.* **2003**, *4*, 599−604.
(37) Wang, H.; Whittaker-Brooks, L.; Fleming, G. R. Exciton and Free Charge Dynamics of Methylammonium Lead Iodide Perovskites Are Different in the Tetragonal and Orthorhombic Phases. *J. Phys. Chem. C* **2015**, *119*, 19590−19595.
(38) Miyata, A.; Mitioglu, A.; Plochocka, P.; Portugall, O.; Wang, J. T. W.; Stranks, S. D.; Snaith, H. J.; Nicholas, R. J. Direct Measurement of the Exciton Binding Energy and Effective Masses for Charge Carriers in Organic-Inorganic Tri-Halide Perovskites. *Nat. Phys.* **2015**, *11*, 582−587.
(39) Even, J.; Pedesseau, L.; Jancu, J. M.; Katan, C. Importance of Spin-Orbit Coupling in Hybrid Organic/Inorganic Perovskites for Photovoltaic Applications. *J. Phys. Chem. Lett.* **2013**, *4*, 2999−3005.
(40) D'Innocenzo, V.; Grancini, G.; Alcocer, M. J. P.; Kandada, A. R. S.; Stranks, S. D.; Lee, M. M.; Lanzani, G.; Snaith, H. J.; Petrozza, A. Excitons Versus Free Charges in Organo-Lead Tri-Halide Perovskites. *Nat. Commun.* **2014**, *5*, 3586.
(41) Tanaka, K.; Takahashi, T.; Ban, T.; Kondo, T.; Uchida, K.; Miura, N. Comparative Study on the Excitons in Lead-Halide-Based Perovskite-Type Crystals Ch3nh3pbbr3ch3nh3pbi3. *Solid State Commun.* **2003**, *127*, 619−623.
(42) Hirasawa, M.; Ishihara, T.; Goto, T.; Uchida, K.; Miura, N. Magnetoabsorption of the Lowest Exciton in Perovskite-Type Compound (Ch3nh3)Pbi3. *Phys. B* **1994**, *201*, 427−430.
(43) Galkowski, K.; Mitioglu, A.; Miyata, A.; Plochocka, P.; Portugall, O.; Eperon, G. E.; Wang, J. T. W.; Stergiopoulos, T.; Stranks, S. D.; Snaith, H. J.; et al. Determination of the Exciton Binding Energy and Effective Masses for Methylammonium and Formamidinium Lead Tri-Halide Perovskite Semiconductors. *Energy Environ. Sci.* **2016**, *9*, 962−970.
(44) Koutselas, I. B.; Ducasse, L.; Papavassiliou, G. C. Electronic Properties of Three- and Low-Dimensional Semiconducting Materials with Pb Halide and Sn Halide Units (Vol. 8, Pg 1217, 1996). *J. Phys.: Condens. Matter* **1996**, *8*, 5953−5953.
(45) Umebayashi, T.; Asai, K.; Kondo, T.; Nakao, A. Electronic Structures of Lead Iodide Based Low-Dimensional Crystals. *Phys. Rev. B: Condens. Matter Mater. Phys.* **2003**, *67*, 155405.
(46) Warman, J. M.; Gelinck, G. H.; de Haas, M. P. The Mobility and Relaxation Kinetics of Charge Carriers in Molecular Materials Studied by Means of Pulse-Radiolysis Time-Resolved Microwave Conductivity: Dialkoxy-Substituted Phenylene-Vinylene Polymers. *J. Phys.: Condens. Matter* **2002**, *14*, 9935−9954.
(47) Warman, J. M.; de Haas, M. P.; Dicker, G.; Grozema, F. C.; Piris, J.; Debije, M. G. Charge Mobilities in Organic Semiconducting Materials Determined by Pulse-Radiolysis Time-Resolved Microwave Conductivity: Pi-Bond-Conjugated Polymers Versus Pi-Pi-Stacked Discotics. *Chem. Mater.* **2004**, *16*, 4600−4609.
(48) Grozema, F. C. Opto-Electronic Properties of Conjugated Molecular Wires. Doctoral Thesis, Delft University of Technology, Delft, The Netherlands, 2003.
(49) Klein, C. A. Bandgap Dependence and Related Features of Radiation Ionization Energies in Semiconductors. *J. Appl. Phys.* **1968**, *39*, 2029−2038.
(50) Alig, R. C.; Bloom, S. Electron-Hole-Pair Creation Energies in Semiconductors. *Phys. Rev. Lett.* **1975**, *35*, 1522−1525.
(51) Klein-Kedem, N.; Cahen, D.; Hodes, G. Effects of Light and Electron Beam Irradiation on Halide Perovskites and Their Solar Cells. *Acc. Chem. Res.* **2016**, *49*, 347−354.
(52) Savenije, T. J.; Ferguson, A. J.; Kopidakis, N.; Rumbles, G. Revealing the Dynamics of Charge Carriers in Polymer:Fullerene Blends Using Photoinduced Time-Resolved Microwave Conductivity. *J. Phys. Chem. C* **2013**, *117*, 24085−24103.
(53) Hutter, E. M.; Eperon, G. E.; Stranks, S. D.; Savenije, T. J. Charge Carriers in Planar and Meso-Structured Organic-Inorganic Perovskites: Mobilities, Lifetimes, and Concentrations of Trap States. *J. Phys. Chem. Lett.* **2015**, *6*, 3082−3090.
(54) Billing, D. G.; Lemmerer, A. Synthesis, Characterization and Phase Transitions in the Inorganic-Organic Layered Perovskite-Type Hybrids [(Cnh2n+1nh3)(2)Pbi4], N = 4, 5 and 6. *Acta Crystallogr., Sect. B: Struct. Sci.* **2007**, *63*, 735−747.
(55) Gélvez-Rueda, M. C.; Cao, D. H.; Patwardhan, S.; Renaud, N.; Stoumpos, C. C.; Schatz, G. C.; Hupp, J. T.; Farha, O. K.; Savenije, T. J.; Kanatzidis, M. G.; et al. Effect of Cation Rotation on Charge Dynamics in Hybrid Lead Halide Perovskites. *J. Phys. Chem. C* **2016**, *120*, 16577−16585.
(56) Straus, D. B.; Parra, S. H.; Iotov, N.; Gebhardt, J.; Rappe, A. M.; Subotnik, J. E.; Kikkawa, J. M.; Kagan, C. R. Direct Observation of Electron-Phonon Coupling and Slow Vibrational Relaxation in Organic-Inorganic Hybrid Perovskites. *J. Am. Chem. Soc.* **2016**, *138*, 13798−13801.
(57) Kitazawa, N.; Aono, M.; Watanabe, Y. Temperature-Dependent Time-Resolved Photoluminescence of (C6h5c2h4nh3)(2)Pbx4 (X = Br and I). *Mater. Chem. Phys.* **2012**, *134*, 875−880.
(58) Hu, T.; Smith, M. D.; Dohner, E. R.; Sher, M. J.; Wu, X. X.; Trinh, M. T.; Fisher, A.; Corbett, J.; Zhu, X. Y.; Karunadasa, H. I.; et al. Mechanism for Broadband White-Light Emission from Two-Dimensional (110) Hybrid Perovskites. *J. Phys. Chem. Lett.* **2016**, *7*, 2258−2263.
(59) Papavassiliou, G. C.; Koutselas, I. B. Structural, Optical and Related Properties of Some Natural Three- and Lower-Dimensional Semiconductor Systems. *Synth. Met.* **1995**, *71*, 1713−1714.
(60) Blancon, J. C.; Tsai, H.; Nie, W.; Stoumpos, C. C.; Pedesseau, L.; Katan, C.; Kepenekian, M.; Soe, C. M. M.; Appavoo, K.; Sfeir, M. Y.; et al. Extremely Efficient Internal Exciton Dissociation through Edge States in Layered 2d Perovskites. *Science* **2017**, *355*, 1288−1291.

DOI: 10.1021/acs.jpcc.7b10705
J. Phys. Chem. C 2017, 121, 26566−26574